THE UNIVERSITY *of* EDINBURGH

Edinburgh Research Explorer

Direct 3D printing of monolithic ion exchange adsorbers

OPEN ACCESS

Direct 3D printing of monolithic ion exchange adsorbers

Ursula Simon & Simone Dimartino*

Institute for Bioengineering, The School of Engineering, The University of Edinburgh,

Edinburgh EH9 3DW, UK.

*Corresponding author: Phone: +44 131 6507305, Email: simone.dimartino@ed.ac.uk

Abstract

Monolithic adsorbers with anion exchange (AEX) properties have been 3D printed in an easy one-step process, i.e. not requiring post-functionalization to introduce the AEX ligands. The adsorber, 3D printed using a commercial digital light processing (DLP) printer, was obtained by copolymerisation of a bifunctional monomer bearing a positively charged quaternary amine as well as an acrylate group, with the biocompatible crosslinker polyethylene glycol diacrylate (PEGDA). To increase the surface area, polyethylene glycol was introduced into the material formulation as pore forming agent. The influence of photoinitiator (Omnirad 819) and photoabsorber (Reactive Orange 16, RO16) concentration was investigated in order to optimize printing resolution, allowing to reliably 3D print features as small as 200 µm and of highly complex Schoen gyroids. Protein binding was measured on AEX adsorbers with a range of ligand densities (0.00, 2.03, 2.60 and 3.18 mmol/mL) using bovine serum albumin (BSA) and c-phycocyanin (CPC) as model proteins. The highest equilibrium binding capacity was found for the material presenting the lowest ligand density analysed (2.03 mmol/mL), adsorbing 73.7 ± 5.9 mg/mL and 38.0 ± 2.2 mg/mL of BSA and CPC, respectively. This novel 3D printed material displayed binding capacities in par or even higher than commercially available chromatographic resins. We expect that the herein presented approach of using bifunctional monomers, bearing commonly used chromatography ligands, will help overcome the material limitations currently refraining 3D printing applications in separation sciences.

Keywords: Additive manufacturing; Digital light processing; 3D print materials;
 Anion exchange chromatography; Protein adsorption

1. Introduction

3D printing, also known as additive manufacturing (AM), encompasses a range of techniques to fabricate three dimensional objects from computer aided design (CAD) models through layer by layer addition of material. Several 3D printing methods have been developed and optimised over the last couple of decades, each with its own specifications in terms of costs, resolution, build size, speed and materials [1]. AM techniques are developing at a fast pace, and today it is possible to print complex structures with high fidelity at micron scale resolution in a rapid and robust process [1]. In addition, the cost of 3D printers is dropping significantly with time, triggering the adoption of AM methods in a range of scientific fields such as chemistry [2], drug delivery [3], microfluidic [4,5]and tissue engineering [6]. Interestingly, 3D printing is not widely employed in the separation sciences yet, especially in chromatographic separations [7]. A range of serious barriers has so far limited the use of 3D printing methods in chromatography, e.g. the lack of materials compatible with both 3D printing processing and chromatographic operations, as well as the relatively poor resolution of current 3D printers to generate features in the micron scale [8].

The performance of chromatographic separations depends on a number of factors, including the flow of the mobile phase within the column and the related axial dispersion and band broadening effects. Traditional stationary phases consist either of random beds of spherical particles or random monolithic networks. Accordingly, each column has a slightly different internal morphology and porous structure, their chromatographic behaviour is impossible to be predicted *a priori*, and they require careful testing and validation of the packing quality prior to use. Computer simulations demonstrated that ordered beds provide significantly improved chromatographic performance over randomly organised stationary phases [9,10]. In an attempt to experimentally prove the simulated results, Fee *et al.* [11] 3D printed chromatography beds with precisely controlled and highly ordered morphology. These were printed with high fidelity and reproducibility to the original CAD designs. 3D printing also opened the opportunity to explore alternative bed configurations and particle shapes, allowing experimental demonstration that spherical particles are not necessarily the best shape for chromatographic operations, and that new bed morphologies can improve pressure drop and plate height characteristics [12]. Yet, only commercially available urethane-based materials for 3D polyjet printing could be tested, and flow performance of the columns was determined by residence time distribution experiments with non-retained tracers. No separation could be carried out as the material did not present suitable functional groups, while its proprietary composition limited opportunity for targeted activation chemistry and functionalization with chromatographic ligands.

Lack of suitable materials for chromatographic separations that can be processed by 3D printers represents the current biggest hurdle for the 3D printing of separation devices. Although, there is a large range of 3D printable materials available on the market (metals, ceramics, polymers), none of it was developed to bear specific functional groups for separations. Additionally, most material formulations are proprietary, and include a range of components such as plasticizers, fillers and additives to enable their 3D printing. This greatly

73 limits any attempt in their functionalization and renders impossible the prediction of their
74 potential separation behaviour.

75 To overcome this issue, three main approaches have been applied to 3D print separation
76 devices. The simplest approach employs commercial materials which show some degree of
77 separation properties. For example, MacDonald *et al.* exploited the overall negative surface
78 charge of the Veroclear material (from Stratasys) to fabricate thin layer chromatography
79 (TLC) platforms for protein separations [13]. Su *et al.* employed another polyacrylate based
80 material (BV-001, Rays Optics Inc.) with electron donor groups on its surface for the
81 fabrication of a device able to selectively extract trace elements from seawater [14].
82 Although this method is relatively straightforward, the lack of knowledge of the material
83 chemistry heavily limits its extension to other separation methods e.g. relying on
84 hydrophobic, multimodal or affinity interactions.

85 A second approach involves the printing of materials with known composition and
86 chemistry, which are functionalised with appropriate chromatographic ligands post printing.
87 This strategy was employed by Fee *et al.* to produce agarose and cellulose based stationary
88 phase which were later functionalized with a range of chromatographic ligands [15]. Seo *et*
89 *al.* printed micropatterned AEX membranes by printing the desired membrane shape with
90 non-functionalised material which was then followed by a quaternisation procedure [16].
91 Such approach is at all similar to current production of chromatographic resins. Albeit it is
92 well established and robust, it requires additional manufacturing steps and adds complexity
93 in the processing line. Functionality can also be achieved by coating 3D printed structures
94 using, for example, initiated chemical vapour deposition [17] or porous metal frameworks
95 [18].

96 The third approach aims at custom design and 3D print the column casing only, which is
97 later packed with commercial adsorber particles [19] or monolithic structures [20]. This
98 approach is particularly original and can lead to column geometries with improved
99 performance [21], but cannot be considered 3D printing of chromatography stationary
100 phases.

101 All these approaches require additional steps than just 3D printing, e.g. material
102 characterisation, post printing functionalisation or the assembly of different parts. On the
103 other hand, direct 3D printing of chromatographic adsorbers, i.e. already containing the
104 desired functional groups, would enable a convenient one-step fabrication method for
105 printing separation devices.

106 3D printing of functional materials has been recently proven in the field of chemical
107 catalysis, where catalytically active structures with carboxylic acid, amine and copper
108 carboxylate functionality were directly printed using bifunctional monomers as building
109 blocks [22]. These bifunctional monomers provided one functional group with the desired
110 catalytic chemistry as well as one to take part in the polymerization reaction. Experiments
111 showed that the performances of the 3D printed catalytic structures were comparable with
112 those of commercial material.

The use of bifunctional monomers has been explored in IEX monoliths by Milton Lee's group. Fully functional porous monoliths were prepared in a single step synthesis via UV initiated polymerisation by copolymerising the crosslinker PEGDA with bifunctional monomers containing sulfonic acid [23,24], phosphoric acid [25], carboxylic acid [26] or amine groups [27]. Porosities were created by the solvents present in the reacting mixture. All produced monoliths showed good protein uptake comparable to commercial columns.

In this work, direct 3D printing was employed to fabricate chromatography stationary phases. The material developed contained AEX moieties, and its formulation was tuned and optimised for their 3D printing in a digital light processing (DLP) 3D printer. Free radical polymerisation between a PEGDA crosslinker and a bifunctional monomer bearing quaternary amine groups was achieved using Omnirad 819 as photoinitiator. Addition of a light absorber was key to tune and control the resolution of the 3D printed models, enabling reliable fabrication of complex structures with 200 µm thick features. The developed AEX material showed excellent protein adsorption behaviour for two model proteins, bovine serum albumin (BSA) and C-Phycocyanin (CPC). Optimal ligand density for protein adsorption was determined by adjusting the composition of the parent formulation before 3D printing. To the best of our knowledge, this work is the first proposing the one-step manufacture of functional stationary phases with perfectly ordered internal morphology.

2. Experimental

2.1. Materials

2-(Acryloyloxy)ethyl trimethylammonium chloride (AETAC, 80 wt. % in water), ethanol (absolute, for HPLC, ≥99.8%), hexamethyldisilazane (HMDS), Reactive Orange 16 (RO16), sodium hydroxide and Sudan I were purchased from Sigma-Aldrich (St. Louis, MO, USA). Bovine serum albumin (protease free powder), isopropanol (IPA, extra pure), polyethylene glycol (PEG-200, average MW 200 g/mol), sodium chloride, sodium phosphate mono and dibasic were obtained from Fisher Scientific (Hampton, NH, USA). Phenyl bis(2,4,6-trimethylbenzoyl)-phosphine oxide (Omnirad 819, former Irgacure 819) was kindly donated by IGM resins (Waalwijk, The Netherlands). Polyethylene glycol diacrylate (PEGDA, SR259, average MW 200 g/mol) was donated from Arkema-Sartomer (Colombes, France). C-Phycocyanin (CPC) was extracted from *Spirulina platensis* and gently provided by Dr. Alistair McCormick (The University of Edinburgh, Institute of Molecular Plant Sciences). All chemicals were used as received; all buffers were prepared using deionised water (EuRO10 Reverse Osmosis System, Evoqua Water Technologies, Pittsburgh, PA, USA).

2.2. Material development

The photocurable material was composed of 60 wt. % PEG-200 as porogen and 40 wt. % PEGDA/AETAC mixture as crosslinker and bifunctional monomer, respectively. Printed samples were created with different ligand densities by adjusting the relative ratio of PEGDA and AETAC (Table 1).

A radical photoinitiator (Omnirad 819, at 0.12, 0.25, 0.5, 1.0 and 1.5 wt. % based on 100 g of porogen-monomers mixture) and a light absorber were added to the mixture. Three dyes

154   were considered as light absorbers to help increase the resolution of the 3D printed models,
155   namely RO16, Sudan I and Tinuvin 326. A NanoDrop 2000c (Fisher Scientific, Hampton, NH,
156   USA) was employed to measure the absorbance spectra of the photoinitiator and
157   photoabsorbers to direct selection of the appropriate light absorber. RO16 was chosen for
158   all further experiments due to its most suitable absorbance spectrum (see Results and
159   Discussion section). Three different concentrations of RO16 (0.063, 0.125, 0.250 wt. %,
160   based on 100 g of porogen-monomers mixture) were tested in combination with 0.5 wt. %
161   Omnirad 819. A final concentration of 0.125 wt. % RO16 was chosen to fabricate the prints
162   (100 µm cure depth at 1.7 s exposure). All material formulations were stored in tubes
163   covered in aluminium foil to prevent spontaneous polymerisation prior to 3D printing.

164   **[Table 1]**

165   ## 2.3.   Model creation and 3D printing
166   Computer-aided design (CAD) models were created on SolidWorks 2015 (Dassault Systèmes
167   SOLIDWORKS Corp., Waltham, MA, USA), exported as STL file and sliced into 2D-layers using
168   Netfabb 2017 (Autodesk, San Rafael, CA, USA). A unit cell of the Schoen Gyroid was created
169   using Mathematica 10.4 (Wolfram Research Inc., Champaign, IL, USA).

170   A Solfex 350 (W2P Engineering, Vienna, Austria) digital light processing (DLP) printer (50 µm
171   pixel size in x-y plane, UV-LED at 385 nm with light intensity of 16 mW/cm^2) was used as 3D
172   printing platform. All parts were printed in 100 µm layers (z-direction) as a reasonable
173   compromise between printing resolution, column size and overall printing time. Post-
174   printing, the parts were washed three times in IPA in an ultrasonic bath (Allendale
175   Ultrasonics, Hodesdon, UK) and then fully cured in water with a xenon Otoflash G171 unit
176   (NK-Optik, Baierbrunn, Germany). Parts were stored in water until final use.

177   To determine the working curve (layer thickness vs exposure time) of the new material
178   formulations, 8 mL of the material were transferred into a petri dish (ø 60 mm) and placed
179   above the printing area of the DLP. Eleven circles (ø 8 mm) were cured at different locations
180   with exposure times from 1 to 60 s. After cleaning with IPA and post-curing, the thickness of
181   the polymerised circles was measured using a micrometre (RS Pro Micrometer External, RS
182   Components, Corby, UK).

183   ## 2.4.   Qualitative characterisation of porous network
184   The internal structure of printed parts was imaged through scanning electron microscopy
185   (SEM, S-4700, Hitachi, Tokyo, Japan). Cylindrical gyroidal structures (50 % external porosity,
186   500 µm wall thickness) were printed and then dehydrated in 70 %, 80 %, 90 % and 100 %
187   ethanol, with each step performed three times for 10 min. The gyroids were then
188   transferred to HMDS for 2 min, HMDS was then removed and samples were left to dry
189   [28,29]. Subsequently, the cylinders were immersed in liquid nitrogen and snapped into
190   halves, gold sputter coated and SEM imaged.

191 The interconnectivity of the porous structure was tested by incubating cylindrical gyroid
192 structures (50% external porosity, 500 µm wall thickness) with 1 mg/mL blue CPC in
193 phosphate buffer (25 mM, pH 7) for 24 h. After incubation, gyroids were cut into halves and
194 the cross section of the walls was visually investigated in regard of colour.

2.5. Protein batch adsorption

196 Hollow cylinders fitting into 96-microplate wells were designed and 3D printed (Figure 1).
197 Prior to protein adsorption tests, printed cylinders were equilibrated with phosphate buffer
198 (25 mM, pH 7) for a minimum of 48 h, with buffer exchange every 12 h. Protein adsorption
199 was triggered by addition of 170 µL phosphate buffer (25 mM, pH 7) containing 0-32 mg/mL
200 BSA or 0-8 mg/mL CPC to each well. The microplates were agitated at 800 rpm using a
201 Thermomixer C (Eppendorf, Hamburg, Germany). Protein adsorption kinetics onto the 3D
202 printed cylinders was calculated by protein uptake in the bulk solution, measuring protein
203 absorbance with a Modulus II Microplate Multimode Reader (Turner BioSystems, Sunnyvale,
204 CA, USA) at regular time intervals. The binding capacity, q, was calculated for each time
205 point using equation (1):

$$q = \frac{(c_i - c) \cdot V}{V_{cylinder}} \tag{1}$$

207 where c_i and c are the initial protein concentration and the concentration at time t,
208 respectively, V is the volume of buffer in the wells and $V_{cylinder}$ is the printed cylinder volume
209 (19.37 µL).

210 The Langmuir model was employed to describe protein loading at equilibrium conditions
211 (q_{eq}) as function of the equilibrium protein concentration in the liquid phase (c_{eq}):

$$q_{eq} = \frac{q_{max} \cdot c_{eq}}{K_D + c_{eq}} \tag{2}$$

213 The maximum binding capacity, q_{max}, and the Langmuir equilibrium coefficient, K_D, were
214 estimated by best fit regression using Origin 2016 (OriginLab, Northampton, MA, USA).

215 BSA concentration was measured through UV readings at 280 nm, while CPC concentration
216 was calculated from the absorbance at 615 and 652 nm according to the expression
217 reported in [30,31], adapted for NanoDrop measurements by adding a correction factor of
218 0.1 to account for the shorter path length:

$$c_{CPC} = \frac{A_{615} - 0.474 \cdot A_{652}}{5.34 \cdot 0.1} \qquad 3$$

220 The absorbance ratio of A_{615}/A_{280} is generally used to describe the purity of CPC. The
221 absorbance at 615 nm corresponds to the maximum absorbance of CPC, whereas the
222 absorbance at 280 nm correlates to contamination with other proteins. A ratio of 0.7 is
223 considered as food grade, 3.9 as reactive grade and greater than 4.0 as analytical grade [32].
224 The CPC applied in experiments had a purity of A_{615}/A_{280} = 2.3. All batch adsorption
225 experiments were performed in triplicate.
226

227 **[Figure 1]**

3. Results & Discussion

3.1. Material development

230 The aim of this study was the one-step 3D printing of chromatographic beds with AEX
231 functionality. This was achieved by UV copolymerisation of the crosslinker PEGDA and the
232 bifunctional monomer AETAC bearing positive charged quaternary amine groups (Figure 2).
233 As second functional group, AETAC displays an acrylate group for the incorporation in the
234 polymeric network. PEGDA was chosen as crosslinker due to its known biocompatibility and
235 low non-specific protein binding [33]. This principle of copolymerisation has previously been
236 reported for the fabrication of ion exchange monoliths [23–27]. In this study, 40 wt. % of the
237 crosslinker-monomer blend was mixed with 60 wt. % PEG-200 as pore forming agent.

238

239 **[Figure 2]**

240

3.1.1. *Optimization of photoinitiator and photoabsorber concentration*

242 The concentration of the photoinitiator in the material formulation determines the
243 thickness of 3D printed layers, commonly known as the cure depth C_D. Different
244 concentrations of the Omnirad 819 photoinitiator were tested and the resulting C_D for an
245 exposure time of 1 and 2 s is summarised in Figure 3a. An exposure time of 1 to 2 s was
246 found to be desirable to ensure an acceptable printing time for monolithic structures in later
247 experiments. At fixed exposure time, the cure depth decreased with increasing
248 photoinitiator concentration. For instance, at 1 s exposure (i.e. a reasonably small exposure
249 time to enable fast printing), C_D was 1456 ± 271 μm when 0.125 wt. % Omnirad 819 was
250 employed, whereas 408 ± 12 μm cured layer was obtained with an eight times higher
251 photoinitiator concentration (1.5 wt. %). At higher photoinitiator concentrations, the
252 supplied light is entirely absorbed in a thinner layer immediately above the print surface,
253 hence limiting light penetration into the photocurable material. Yet, the thinnest printed
254 layer achieved at the highest photoinitiator concentration of 1.5 wt. % (limited by the
255 solubility of Omnirad 819 in the monomers/porogen mixture) was 408 ± 12 μm for an
256 exposure time of 1 s. Such layer thickness was considered too large for appropriate
257 resolution in the 3D printed models; in addition, formulations with high initiator
258 concentrations are extremely sensitive to light, and start polymerizing before the 3D
259 printing process is initiated, thus making its handling particularly delicate. On the other
260 hand, C_D can be reduced by shortening the exposure time, however, extremely short
261 exposure times are not reliably delivered by the light engine of the DLP printer. The required
262 exposure time to cure a 100 μm layer was estimated equal to 64 ms or 344 ms for the
263 materials containing 0.25 wt. % or 1.5 wt. % Omnirad 819, respectively (estimation using
264 fitting parameters from Table S2). A reasonable compromise of 0.5 wt. % Omnirad 819 was
265 selected to prepare all material formulations.

266

267 **[Figure 3]**

268

Light absorbers (or photoabsorbers, PA) are usually added to the formulation to increase control over the polymerization reaction and further decrease the cure depth. These components absorb part of the supplied light, thus lowering the penetration depth of the UV light within the material, hence reducing C_D. Figure 3b presents the absorbance spectra of three light absorbers considered in this work, RO16, Tinuvin 326 and Sudan I. All three PAs absorb light at 385 nm, i.e. the printer's output. Tinuvin 326 absorbed up to 410 nm, whereas the photoinitiator (Omnirad 819) absorbed up to 440 nm. Accordingly, Tinuvin 326 is unable to protect the formulation from early polymerisation in ambient light. Sudan I and RO16 showed similar absorbance spectra, overlapping completely with the Omnirad 819 spectrum in the UV-vis range, hence ensuring full protection in ambient light. For further investigations RO16 was chosen due to its lower health and safety risks.

Working curves *(C_D vs. exposure time)* for different RO16 concentrations in combination with 0.5 wt. % Omnirad 819 are shown in Figure 3c. As expected, use of higher concentrations of the PA resulted in thinner polymerised layers. The appropriate concentration of PA to be used is a compromise between its concentration in the formulation and the exposure time required to achieve a certain cure depth, i.e. an appropriate resolution of the printed part. On one hand, concentration should be as small as possible to limit its presence in the cured model part, which in turn could cause secondary issues such as non-specific protein binding and colour retention. On the other hand, light exposure should enable curing of a layer in a reasonable time and with reasonable resolution. As stated earlier, the target in this work was the printing of 100 μm layers in 1 - 2 s. At the smallest RO16 concentration tested (0.06 wt. %), an exposure time of 1 s resulted in a C_D of 286 ± 31 μm, i.e. a 30 % reduction with respect to the parent formulation with no PA. At 0.25 wt. % RO16, 1 s exposure did not cure a measurable layer, and approximately 2.4 s would be required to cure a 100 μm thick layer (according to logarithmic fit). An intermediate concentration of 0.125 wt. % RO16 led to a C_D of 100 ± 30 μm in 1 s UV exposure, equivalent to a 75 % reduction with respect to the formulation with no PA. This concentration was employed in all further formulations and experiments.

3.1.2. Printability and resolution of the new material formulation

To investigate the printability and resolution of the material formulation here developed, a test cube was designed and 3D printed (Figure 4a and b). The cube contains square channels of 500 μm width separated by walls with thickness ranging from 200 to 1000 μm. The design of the test cube is symmetrical and such that resolution over all three printing directions (*x*, *y* and *z*) can be investigated at the same time, regardless of the orientation of the cube. As can be observed in Figure 4b, all walls were neatly printed, demonstrating the ability to reliably print up to 200 μm thin features, i.e. two 100 μm printed layers.

Conventional IEX adsorber beads for preparative chromatography have diameters ranging from 15 to 200 μm, with average diameter of 90 μm [34]. The structures 3D printed with the new IEX material have feature size comparable with those of commercial chromatographic resins. Yet, this study aims at presenting the proof the concept of direct printing of

310 functional materials for IEX. Further increase of the print resolution (50 to 100 μm range) is
311 currently being investigated and will be the focus of future reports.
312 The capability of 3D printing technologies to enable manufacturing of optimized three
313 dimensional ordered structures has been recently discussed [8,10,12]. In particular, printing
314 of complex monolithic structures with defined channel size, geometry and configuration
315 tuned for specific separations is particularly attractive. Triply periodic minimal surfaces
316 (TMPS) have been recently reported as geometries for chromatographic beds, with
317 computer simulations demonstrating superior chromatographic performance in terms of
318 permeability and axial dispersion (HETP) over random packed beds and monoliths [10]. The
319 potential to print these complex TPMS geometries using the novel material formulation was
320 demonstrated (Figure 4c-f). The complex Schoen Gyroid structure, designed with 50 %
321 external porosity and 500 μm wall thickness, was reliably and accurately printed, with
322 interconnected walls for mechanical strength and no occluded channels for fluid flow. These
323 printed cylinders can be easily introduced into traditional chromatography columns and
324 connected to chromatography systems (e.g. FPLC) for chromatographic separations. As
325 printer resolution is addressed, TPMS structures with smaller features will be able to be
326 printed and employed.
327
328 **[Figure 4]**
329
330 *3.1.3. Qualitative study of material porosity*
331 The formulation of the new material incorporated PEG-200 as pore forming agent. The
332 porous network within the printed material could not be analysed by SEM as the drying
333 operations for sample preparation caused substantial shrinkage and collapse of the porous
334 structure. As an alternative to SEM, the porous structure and its interconnectivity was
335 qualitatively tested by incubation of the gyroid model in CPC (Figure 4f-h), a blue protein
336 pigment complex extracted from the cyanobacterium *Spirulina platensis.* After 24 h
337 incubation, the original orange colour due to the RO16 dye was completely concealed by the
338 blue characteristic of CPC (Figure 4f and g). The cylinder was cut open to demonstrate
339 diffusion of the CPC protein within the bulk of the walls, with strong blue staining of the cut
340 sections (Figure 4h). As a result, it was concluded that the pores within the polymerised
341 network were, on average, larger than the diameter of the CPC protein complex (11 nm)
342 [35] and that the pores were highly interconnected. Typical soluble proteins have a
343 diameter of 3 - 6 nm [36], suggesting that the internal porous network is suitable for protein
344 adsorption. Further quantitative work on the porosity characteristics of the 3D printed
345 materials is required, both to improve the current material in terms of protein adsorption,
346 but also to enable use of this material towards other separation targets such as DNA and
347 viruses (VLPs, viral vectors, etc.).

348 **3.2.   Protein batch adsorption**
349 Batch adsorption experiments were performed to analyse the protein adsorption behaviour
350 of the novel material formulations. The advantage of 3D printing to fabricate three
351 dimensional shapes from CAD models was employed here to simplify execution of the

352   experiments. In particular, the adsorbers were designed as hollow cylinders with 5 mm
353   outer diameter and 3.5 mm height as to fit in a well of a UV transparent 96-well plate
354   (Figure 1). The walls of the cylinders had a thickness of 500 μm to ensure sufficient
355   mechanical properties, and presented a number of holes to facilitate mixing of the buffers
356   and protein solutions.

357   In batch adsorption experiments with traditional chromatographic beads, protein
358   concentration is measured by withdrawal of a small amount of solution followed by
359   spectrophotometry. This method requires careful handling or a robotic platform, and
360   inherently introduce experimental errors due to the change of the overall volume of buffer
361   throughout the experiment. This is particularly true in kinetic essays, i.e. where protein
362   concentration has to be monitored frequently. The hollow cylinder design here proposed,
363   enabled by 3D printing, allowed to measure protein concentration using a simple plate
364   reader, with no need to either remove the adsorber from the wells or withdrawal of the
365   protein solutions, greatly simplifying execution of the experiments.

366   The effect of ligand density on protein adsorption was preliminary tested using BSA as
367   model protein. Four different material compositions, corresponding to ligand densities of
368   quaternary amine functionality of 0.00 (control), 2.03, 2.60 and 3.18 mmol/mL, were
369   prepared and printed in the hollow cylinder format. BSA is considerably smaller than CPC
370   [37], thus it is reasonable to assume that the material's internal porous structure is
371   accessible to BSA. Figure 5a presents the BSA binding kinetics onto the AEX material with a
372   ligand density of 2.03 mmol/mL (kinetics for the materials with 2.60 and 3.18 mmol/mL
373   ligand density can be found in Fig. S2). The adsorption kinetics was relatively fast, reaching
374   equilibrium conditions after a few hours only (dependent on initial BSA concentration). In
375   particular, at the lowest concentrations tested, equilibrium is reached after 1-3 hours, while
376   equilibrium was reached in less than 24 h at the highest BSA concentration tested.
377   Commercial bead based chromatography resins generally reach equilibrium within a couple
378   of hours [31,38–40], however, their characteristic dimension for diffusion (i.e. bead size) is
379   about 10 times shorter than the 3D printed cylinder walls (500 μm). The adsorption kinetics
380   observed results from a combination of different mass transport mechanisms, including
381   boundary layer mass transfer, diffusion within the internal pores, and adsorption kinetics.
382   The relatively thick walls of the cylindrical adsorbers (500 μm) suggests that diffusional
383   resistance might be the limiting factor for adsorption. This is particularly true at higher
384   protein concentrations, i.e. where diffusion may be hindered by previously adsorbed protein
385   molecules.

386   Equilibrium adsorption isotherms were measured using the data obtained after 24 h
387   incubation (Figure 5b). The Langmuir model was employed to best-fit the adsorption
388   isotherms, with model parameter summarized in Table 2. The highest binding capacity of
389   73.7 ± 5.9 mg/mL was achieved with ligand density of 2.03 mmol/mL. Higher ligand densities
390   resulted in significantly lower binding capacities (57.4 ± 2.6 and 23.3 ± 2.5 mg/mL for 2.60
391   and 3.18 mmol/mL ligand density), indicating lower pore diffusivity and ligand accessibility
392   as the ligand density increases. Similar trends of protein binding capacity with ligand density

393 are relatively common [41,42] and justify the need to determine the optimum ligand density
394 when a new material is being developed. It is not excluded that lower ligand densities may
395 lead to improved binding characteristics for pre-functionalized 3D printed materials. The
396 control adsorber, i.e. 3D printed without functional monomer, showed detectable albeit low
397 non-specific protein adsorption (less than 10% with respect to the material with
398 2.03 mmol/mL ligand density) in agreement with other research findings [33]. Low non-
399 specific binding is a desirable characteristic for stationary phases, supporting the use of the
400 herein developed material as monolithic adsorbent for chromatography.

401 Commercial chromatographic resins with quaternary amine functional groups show
402 equilibrium binding capacities of over 100 mg/mL for BSA. For example, Streamline Q XL
403 media from GE Healthcare, a resin for expanded bed adsorption chromatography, has
404 maximum binding capacity of 170 ± 5 mg/mL and equilibrium coefficient of 8 ± 4 mg/mL for
405 BSA [43]. Q-Sepharose FF, another AEX resin from GE Healthcare, displays a maximum
406 binding capacity of 102.4 ± 1.6 mg/mL and an equilibrium coefficient of 0.109 ± 0.011
407 mg/mL [44]. Both resins bear a tenfold lower ligand density than material developed in this
408 work [45,46]. That supports the earlier observation that lower ligand densities may lead to
409 increased binding capacities. Other chromatographic media, such as membranes and
410 monoliths, instead display capacities in the 25-40 mg/ml range. For instance, the Sartorius's
411 Q membrane has a reported maximum capacity of 27.7 mg/mL [47] for a ligand density of
412 0.18 - 0.24 mmol/mL [48], while BIA CIM-QA monoliths are endowed with dynamic binding
413 capacities of 30-40 mg/mL for BSA [49] and ligand densities of about 1.1 mmol/mL [50]. Li *et*
414 *al*. prepared an AEX monolith using similar chemistry as described in this work and reported
415 a dynamic binding capacity of 56 mg/mL for a ligand density of 2.63 mmol/mL [27],
416 comparable to the material with intermediate ligand density presented in this work (note Li
417 *et al*. determined binding capacity in dynamic conditions). The novel 3D-printable material
418 here presented displays somewhat lower binding capacity than traditional bead based
419 resins (approx. 0.4 times than Streamline Q XL and 0.7 times than Q-Sepharose), but
420 significantly higher than membranes and monoliths. These results are extremely promising,
421 considering this is the first reported attempt to develop a pre-functional 3D printable
422 material for chromatography. Optimisation of the material's composition, ligand density and
423 separation conditions has great potential to improve the adsorption performance of such
424 3D printable materials.

425 **[Figure 5]**
426

427 The best performing material with 2.03 mmol/mL ligand density was selected for further
428 adsorption experiments with CPC. Its strong blue colour facilitated visual observation of the
429 adsorption process with time, with apparent colour changes of both the protein solution
430 and the adsorber cylinders. In particular, a noticeable decrease in colour of the supernatant
431 was observed for all CPC concentrations investigated (Figure 6a). At the same time, the
432 adsorber cylinders turned from the initial orange colour to blue (Figure 6b), with stronger

433   blue shade at higher CPC concentrations. This visually proved successful adsorption, with
434   transfer of the protein from the liquid to the solid phase.

435   Protein adsorption was quantitatively confirmed by spectrophotometry, with equilibrium
436   adsorption data of CPC onto the newly developed AEX material summarized in Figure 6c and
437   best-fit Langmuir parameters in Table 2. Data for CPC adsorption onto quaternary amine
438   resins is particularly scarce in the literature, limiting the comparison between different
439   chromatographic materials. The only data equilibrium data for CPC adsorption available are
440   for the Streamline Q XL [38] and Q Sepharose FF [31] (extracted from [38] and [31] and
441   reported in Figure 6 c to ease comparison). As opposite to what observed with adsorption of
442   BSA, the novel 3D printed AEX material displayed higher CPC adsorption capacity than the
443   commercial AEX resins, namely 1.4 times and 1.7 higher q_{max} for Streamline Q XL and Q-
444   Sepharose, respectively. The affinity towards the CPC protein complex is on the same order
445   of magnitude for the three materials, with the 3D printed adsorber having slightly better
446   affinity compared to Streamline Q-XL (halved k_D) and very similar to Q-Sepharose.

447
448   **[Figure 6]**
449

450   Interestingly, the adsorption capacity significantly drops from BSA to CPC, irrespective of the
451   material considered. However, while the drop-in binding capacity from BSA to CPC was a
452   dramatic 83 % in the Streamline Q XL and 78% in Q-Sepharose material, it only dropped of
453   40 % in the 3D printed AEX material. This difference is not related solely to the different
454   properties of the two proteins such as their difference in size (67 kDA BSA [44] vs. 112 kDa
455   CPC [51]), their isoelectric point (4.9 for BSA [44] vs. 5.8 for CPC [52]) and the distribution of
456   charged and hydrophobic patches on the outer protein shell, but also to the material
457   properties e.g. ligand density, size and interconnectivity of internal porous structure. This
458   observation highlights, again, the importance of material optimization towards the specific
459   target protein of interest. Current work is targeting material optimisation in regard of
460   porous structure, ligand density and mechanical properties. Other than optimization of
461   material properties, inherent matter for researchers in the material and separation sciences,
462   3D printing enables the tuning of the geometry for the stationary phase as well as the
463   mobile phase, thus offering an additional factor for further process optimization.

464   **[Table 2]**

465   ## 4. Conclusions

466   This work demonstrates, for the first time, the potential to directly 3D print fully functional
467   stationary phases for protein separations in one simple manufacturing step. In particular,
468   anion exchange adsorbers were fabricated from a 3D printable material formulation
469   comprising i) a bifunctional monomer bearing quaternary amine groups as AEX ligands, ii) a
470   crosslinker to impart mechanical stability to the polymeric network, iii) a photoinitiator to
471   trigger the polymerization reaction upon exposure to UV light, iv) a pore forming agent to

472 increase the surface area of the resulting stationary phase, and v) a photoabsorber to
473 increase the resolution of the 3D printed part. This mixture enabled 3D printing of complex
474 structures such as the Schoen gyroid with high fidelity, as well as to fabricate parts with
475 200 μm large features. Even though this feature size is on the top range of commercial
476 chromatography resins, upcoming developments in 3D printing technologies are expected
477 to bring the resolution below the 100 μm threshold.

478 3D printed anion exchange structures were tested for adsorption of BSA and CPC, revealing
479 excellent adsorption characteristics, in line or even superior than those of commercially
480 available quaternary amine adsorbers. It is worth noting that such results were obtained
481 after a basic optimization of the material composition and 3D printing settings. Additional
482 optimization efforts, e.g. on the porous structure of the cured material, print resolution, and
483 material formulation, has the potential to further improve the adsorption characteristics of
484 such 3D printable AEX chromatographic materials. Also, use of other bifunctional monomers
485 enables extension of this approach to fabricate columns that could operate in other
486 chromatographic modes. For example, 2-carboxyethyl acrylate [26] and sulfopropyl
487 methacrylate [23] could produce cation exchange materials, while butyl methacrylate and 2-
488 hydroxyethyl methacrylate could be part of the formulation to fabricate hydrophobic
489 interaction columns [53].

490 The capability of 3D printing to create complex three-dimensional models directly from CAD
491 designs was exemplified in this work. Adsorbers were designed and 3D printed as hollow
492 cylinders, significantly simplifying execution of batch adsorption experiments in 96 well
493 plate format. This concept can be extrapolated in the future, with columns designed and
494 fabricated with new internal geometries, with improved chromatographic characteristics to
495 suit specific separation and purification applications.

496 We believe the results presented here enable the first steps to overcome the current
497 limitation in terms of materials compatible with 3D printing operations and at the same
498 time suitable for chromatographic separations. This has the potential to revolutionise the
499 chromatography arena, with fine-tuned and robust columns locally 3D printed, on demand
500 and over a short period of time (e.g. overnight) as opposed to the current paradigm of "one-
501 column-fits-all-applications" produced in centralized manufacturing facilities.

502

508

6. References

[1] S.C. Ligon, R. Liska, J. Stampfl, M. Gurr, R. Mülhaupt, Polymers for 3D Printing and Customized Additive Manufacturing, Chem. Rev. 117 (2017) 10212–10290. doi:10.1021/acs.chemrev.7b00074.

[2] B. Gross, S.Y. Lockwood, D.M. Spence, Recent advances in analytical chemistry by 3D printing, Anal. Chem. 89 (2017) 57–70. doi:10.1021/acs.analchem.6b04344.

[3] J. Goole, K. Amighi, 3D printing in pharmaceutics: A new tool for designing customized drug delivery systems, Int. J. Pharm. 499 (2016) 376–394. doi:10.1016/j.ijpharm.2015.12.071.

[4] N. Bhattacharjee, A. Urrios, S. Kang, A. Folch, The upcoming 3D-printing revolution in microfluidics, Lab Chip. 16 (2016) 1720–1742. doi:10.1039/C6LC00163G.

[5] C. Chen, B.T. Mehl, A.S. Munshi, A.D. Townsend, D.M. Spence, R.S. Martin, 3D-printed microfluidic devices: fabrication, advantages and limitations—a mini review, Anal. Methods. 8 (2016) 6005–6012. doi:10.1039/C6AY01671E.

[6] W. Zhu, X. Ma, M. Gou, D. Mei, K. Zhang, S. Chen, 3D printing of functional biomaterials for tissue engineering, Curr. Opin. Biotechnol. 40 (2016) 103–112. doi:10.1016/j.copbio.2016.03.014.

[7] U. Kalsoom, P.N. Nesterenko, B. Paull, Current and future impact of 3D printing on the separation sciences, TrAC - Trends Anal. Chem. 105 (2018) 492–502. doi:10.1016/j.trac.2018.06.006.

[8] C. Salmean, S. Dimartino, Chromatographic Stationary Phases with Ordered Morphology: State of the Art and Future Development, Chromatographia. (n.d.). doi:submitted.

[9] M.R. Schure, R.S. Maier, D.M. Kroll, H.T. Davis, Simulation of ordered packed beds in chromatography, J. Chromatogr. A. 1031 (2004) 79–86. doi:10.1016/j.chroma.2003.12.030.

[10] F. Dolamore, C. Fee, S. Dimartino, Modelling ordered packed beds of spheres: The importance of bed orientation and the influence of tortuosity on dispersion, J. Chromatogr. A. 1532 (2018) 150–160. doi:10.1016/j.chroma.2017.12.004.

[11] C. Fee, S. Nawada, S. Dimartino, 3D printed porous media columns with fine control of column packing morphology, J. Chromatogr. A. 1333 (2014) 18–24. doi:10.1016/j.chroma.2014.01.043.

[12] S. Nawada, S. Dimartino, C. Fee, Dispersion behavior of 3D-printed columns with homogeneous microstructures comprising differing element shapes, Chem. Eng. Sci. 164 (2017) 90–98. doi:10.1016/j.ces.2017.02.012.

[13] N.P. Macdonald, S.A. Currivan, L. Tedone, B. Paull, Direct Production of Microstructured Surfaces for Planar Chromatography Using 3D Printing, Anal. Chem. 89 (2017) 2457–2463. doi:10.1021/acs.analchem.6b04546.

[14] C.K. Su, P.J. Peng, Y.C. Sun, Fully 3D-Printed Preconcentrator for Selective Extraction of Trace Elements in Seawater, Anal. Chem. 87 (2015) 6945–6950. doi:10.1021/acs.analchem.5b01599.

[15] C.J. Fee, S. Dimartino, T. Huber, Separation medium, WO2017103863A1, 2016. https://patents.google.com/patent/WO2017103863A1/pt (accessed September 24,

552   2018).

553   [16] J. Seo, D.I. Kushner, M.A. Hickner, 3D Printing of Micro-patterned Anion Exchange
554   Membranes, ACS Appl. Mater. Interfaces. (2016) acsami.6b03455.
555   doi:10.1021/acsami.6b03455.

556   [17] C. Cheng, M. Gupta, Surface functionalization of 3D-printed plastics via initiated
557   chemical vapor deposition, Beilstein J. Nanotechnol. 8 (2017) 1629–1636.
558   doi:10.3762/bjnano.8.162.

559   [18] Z. Wang, J. Wang, M. Li, K. Sun, C. Liu, Three-dimensional Printed Acrylonitrile
560   Butadiene Styrene Framework Coated with Cu-BTC Metal-organic Frameworks for the
561   Removal of Methylene Blue, Sci. Rep. 4 (2015) 5939. doi:10.1038/srep05939.

562   [19] S. Sandron, B. Heery, V. Gupta, D.A. Collins, E.P. Nesterenko, P.N. Nesterenko, M.
563   Talebi, S. Beirne, F. Thompson, G.G. Wallace, D. Brabazon, F. Regan, B. Paull, 3D printed
564   metal columns for capillary liquid chromatography, T[1] S. Sandron, B. Heery, V. Gupta,
565   D.A. Collins, E.P. Nesterenko, P.N. Nesterenko, M. Talebi, S. Beirne, F. Thompson, G.G.
566   Wallace, D. Brabazon, F. Regan, B. Paull, 3D Print. Met. Columns Capill. Liq.
567   Chromatogr. Anal. 139 6343–6. 139 (2014) 6343–6347. doi:10.1039/C4AN01476F.

568   [20] V. Gupta, M. Talebi, J. Deverell, S. Sandron, P.N. Nesterenko, B. Heery, F. Thompson, S.
569   Beirne, G.G. Wallace, B. Paull, 3D printed titanium micro-bore columns containing
570   polymer monoliths for reversed-phase liquid chromatography, Anal. Chim. Acta. 910
571   (2016) 84–94. doi:10.1016/j.aca.2016.01.012.

572   [21] V. Gupta, S. Beirne, P.N. Nesterenko, B. Paull, Investigating the Effect of Column
573   Geometry on Separation Efficiency using 3D Printed Liquid Chromatographic Columns
574   Containing Polymer Monolithic Phases, Anal. Chem. 90 (2018) 1186–1194.
575   doi:10.1021/acs.analchem.7b03778.

576   [22] J.S. Manzano, Z.B. Weinstein, A.D. Sadow, I.I. Slowing, Direct 3D Printing of Catalytically
577   Active Structures, ACS Catal. 7 (2017) 7567–7577. doi:10.1021/acscatal.7b02111.

578   [23] X. Chen, H.D. Tolley, M.L. Lee, Polymeric strong cation-exchange monolithic column for
579   capillary liquid chromatography of peptides and proteins, J. Sep. Sci. 32 (2009) 2565–
580   2573. doi:10.1002/jssc.200900255.

581   [24] B. Gu, Y. Li, M.L. Lee, Polymer monoliths with low hydrophobicity for strong cation-
582   exchange capillary liquid chromatography of peptides and proteins, Anal. Chem. 79
583   (2007) 5848–5855. doi:10.1021/ac0623585.

584   [25] X. Chen, H.D. Tolley, M.L. Lee, Polymeric cation-exchange monolithic columns
585   containing phosphoric acid functional groups for capillary liquid chromatography of
586   peptides and proteins, J. Chromatogr. A. 1217 (2010) 3844–3854.
587   doi:10.1016/j.chroma.2010.04.032.

588   [26] X. Chen, H.D. Tolley, M.L. Lee, Weak cation-exchange monolithic column for capillary
589   liquid chromatography of peptides and proteins, J. Sep. Sci. 34 (2011) 2063–2071.
590   doi:10.1002/jssc.201100156.

591   [27] Y. Li, B. Gu, H. Dennis Tolley, M.L. Lee, Preparation of polymeric monoliths by
592   copolymerization of acrylate monomers with amine functionalities for anion-exchange
593   capillary liquid chromatography of proteins, J. Chromatogr. A. 1216 (2009) 5525–5532.
594   doi:10.1016/j.chroma.2009.05.037.

595   [28] L. Brigo, A. Urciuolo, S. Giulitti, G. Della Giustina, M. Tromayer, R. Liska, N. Elvassore,

G. Brusatin, 3D high-resolution two-photon crosslinked hydrogel structures for biological studies, Acta Biomater. 55 (2017) 373–384. doi:10.1016/j.actbio.2017.03.036.

[29] F. Braet, R. De Zanger, E. Wisse, Drying cells for SEM, AFM and TEM by hexamethyldisilazane: A study on hepatic endothelial cells, J. Microsc. 186 (1997) 84–87. doi:10.1046/j.1365-2818.1997.1940755.x.

[30] A. Bennett, L. Bogorad, Complementary chromatic adaption in a filamentous blue-green alga, J. Cell Biol. 58 (1973) 419–435. doi:10.1083/jcb.58.2.419.

[31] S.T. Silveira, L.K. De Menezes Quines, C.A.V. Burkert, S.J. Kalil, Separation of phycocyanin from Spirulina platensis using ion exchange chromatography, Bioprocess Biosyst. Eng. 31 (2008) 477–482. doi:10.1007/s00449-007-0185-1.

[32] M. Rito-Palomares, L. Nuez, D. Amador, Practical application of aqueous two-phase systems for the development of a prototype process for c-phycocyanin recovery from Spirulina maxima, J. Chem. Technol. Biotechnol. 76 (2001) 1273–1280. doi:10.1002/jctb.507.

[33] B. Gu, J.M. Armenta, M.L. Lee, Preparation and evaluation of poly(polyethylene glycol methyl ether acrylate-co-polyethylene glycol diacrylate) monolith for protein analysis, J. Chromatogr. A. 1079 (2005) 382–391. doi:10.1016/j.chroma.2005.02.088.

[34] GE Healthcare, Ion Exchange Chromatography: Principles and Methods, GE Healthcare Bio-Sciences AB, Uppsala Sweden, 2016.

[35] R.G. Fisher, N.E. Woods, H.E. Fuchs, R.M. Sweet, Three-dimensional structures of C-phycocyanin and B-phycoerythrin at 5-A resolution., J. Biol. Chem. 255 (1980) 5082–5089.

[36] R. Milo, R. Phillips, Cell Biology by the Numbers, 1st ed., Garland Science, 2015.

[37] C.C. Striemer, T.R. Gaborski, J.L. McGrath, P.M. Fauchet, Charge- and size-based separation of macromolecules using ultrathin silicon membranes, Nature. 445 (2007) 749–753. doi:10.1038/nature05532.

[38] L. Sala, F.S. Figueira, G.P. Cerveira, C.C. Moraes, S.J. Kalil, Kinetics and adsorption isotherm of C-Phycocyanin from Spirulina platensis on ion-exchange resins, Brazilian J. Chem. Eng. 31 (2014) 1013–1022. doi:10.1590/0104-6632.20140314s00002443.

[39] G. Carta, A. Ubiera, Particle-size distribution effects in batch adsorption, AIChE J. 49 (2003) 3066–3073. doi:10.1002/aic.690491208.

[40] S. Zhang, Y. Sun, Study on protein adsorption kinetics to a dye-ligand adsorbent by the pore diffusion model, J. Chromatogr. A. 964 (2002) 35–46. doi:10.1016/S0021-9673(02)00665-9.

[41] A. Franke, N. Forrer, A. Butté, B. Cvijetić, M. Morbidelli, M. Jöhnck, M. Schulte, Role of the ligand density in cation exchange materials for the purification of proteins, J. Chromatogr. A. 1217 (2010) 2216–2225. doi:10.1016/j.chroma.2010.02.002.

[42] K. Wrzosek, M. Gramblička, M. Polakovič, Influence of ligand density on antibody binding capacity of cation-exchange adsorbents, J. Chromatogr. A. 1216 (2009) 5039–5044. doi:10.1016/j.chroma.2009.04.073.

[43] J. Thömmes, Investigations on protein adsorption to agarose-dextran composite media, Biotechnol. Bioeng. 62 (1999) 358–362. doi:10.1002/(SICI)1097-

639   0290(19990205)62:3<358::AID-BIT12>3.0.CO;2-9.

[44]   J. Liang, G. Fieg, Q.H. Shi, Y. Sun, Single and binary adsorption of proteins on ion-
       exchange adsorbent: The effectiveness of isothermal models, J. Sep. Sci. 35 (2012)
       2162–2173. doi:10.1002/jssc.201200101.

[45]   STREAMLINE   Q   XL   -   GE   Healthcare   Life   Sciences,   (n.d.).
       https://www.gelifesciences.com/en/es/shop/streamline-q-xl-p-02151#tech-spec-
       table (accessed November 15, 2018).

[46]   Q   Sepharose   Fast   Flow   -   GE   Healthcare   Life   Sciences,   (n.d.).
       https://www.gelifesciences.com/en/es/shop/chromatography/resins/ion-
       exchange/q-sepharose-fast-flow-p-04285#tech-spec-table (accessed November 15,
       2018).

[47]   S.E. Bower, S.R. Wickramasinghe, Elimination of non-uniform, extra-device flow effects
       in   membrane   adsorbers,   J.   Memb.   Sci.   330   (2009)   379–387.
       doi:10.1016/j.memsci.2009.01.020.

[48]   Sartobind® Q A4 Sheet | Membrane Chromatography | Laboratory | Products | PCM
       Categories | Satorius   Root | Sartorius   Site   WW,   (n.d.).
       https://www.sartorius.com/shop/ww/en/usd/pcm-
       categories/products/laboratory/membrane-chromatography/sartobind®-q-a4-
       sheet/p/94IEXQ42-001 (accessed November 15, 2018).

[49]   J.A. Iberer G., Hahn R., Monoliths as stationary phases for separating biopolymers--
       fourth-generation chromatography sorbents, LC-GC. 17 (1999) 998–1005.

[50]   M. Bencina, A. Podgornik, A. Strancar, Characterization of methacrylate monoliths for
       purification   of   DNA   molecules,   J.   Sep.   Sci.   27   (2004)   801–810.
       doi:10.1002/jssc.200401784.

[51]   A. Patel, S. Mishra, R. Pawar, P.K. Ghosh, Purification and characterization of C-
       Phycocyanin from cyanobacterial species of marine and freshwater habitat, Protein
       Expr. Purif. 40 (2005) 248–255. doi:10.1016/j.pep.2004.10.028.

[52]   A. Narayan, K. Raghavarao, Extraction and Purification of C-Phycocyanin from Spirulina
       Platensis Employing Aqueous Two Phase Systems, Int. J. Food Eng. 3 (2007).
       doi:10.2202/1556-3758.1105.

[53]   P. Hemström, A. Nordborg, K. Irgum, F. Svec, J.M.J. Fréchet, Polymer-based monolithic
       microcolumns for hydrophobic interaction chromatography of proteins, J. Sep. Sci. 29
       (2006) 25–32. doi:10.1002/jssc.200500239.

673 **7. Tables**
674

675 Table 1: Composition of the different resin formulations.

| Ligand density [mmol/mL]	AETAC [wt. %]	PEGDA [wt. %]	PEG-200 [wt. %]
0	0	40	60
2.03	14	26	60
2.60	18	22	60
3.18	22	18	60

676

677

678 Table 2: Langmuir parameters for BSA and CPC adsorption onto the novel 3D printed material in comparison to commercial chromatography
679 resins. Displayed errors correspond to standard error.

		3D printed material			Streamline Q XL	Q Sepharose FF	Sartorius Q membrane
		2.03 mmol/mL	2.60 mmol/mL	3.18 mmol/mL	0.23 - 0.33 mmol/mL [45][1]	0.18- 0.24 mmol/mL [46][1]	0.07 – 0.18 mmol/mL [48][2]
BSA	q_{max} [mg/mL]	73.7 ± 5.9	57.4 ± 2.6	23.3 ± 2.5	170 ± 5	102.4 ± 1.6[3]	27.2
	k_D [mg/mL]	0.381 ± 0.108	0.274 ± 0.048	0.128 ± 0.075	8 ± 4	0.109 ± 0.011[3]	0.054
	R^2	0.92	0.98	0.75	-	-	0.99
	Data source	This work	This work	This work	[43]	[44]	[47]
CPC	q_{max}	38.0 ± 2.2			28.1 ± 0.1	22.7	
	k_D	0.041 ± 0.010			0.082 ± 0.001	0.031	
	R^2	0.97			0.96	0.98	
	Data source	This work			[38]	[31]	

[1] Data given in mmol Cl^-/mL, assumed same molar concentration between Cl^- and Q-ligand
[2] Data given in µeq/cm², assumed normal concentration equals to molar concentration, converted to mmol/mL using membrane thickness of 275 µm [47]
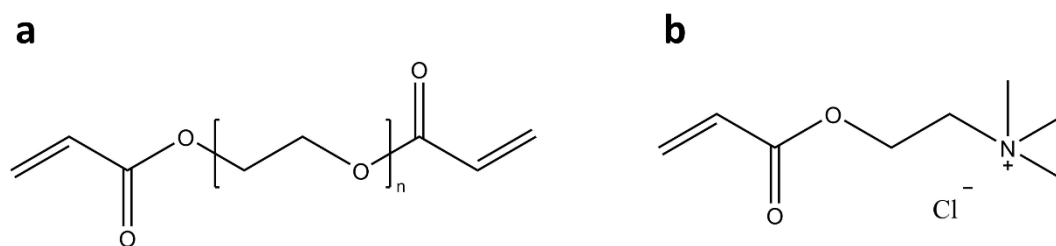[3] Data given in mmoL/L, converted to mg/mL using molecular weight of BSA (67 kDa).

680

Figure captions
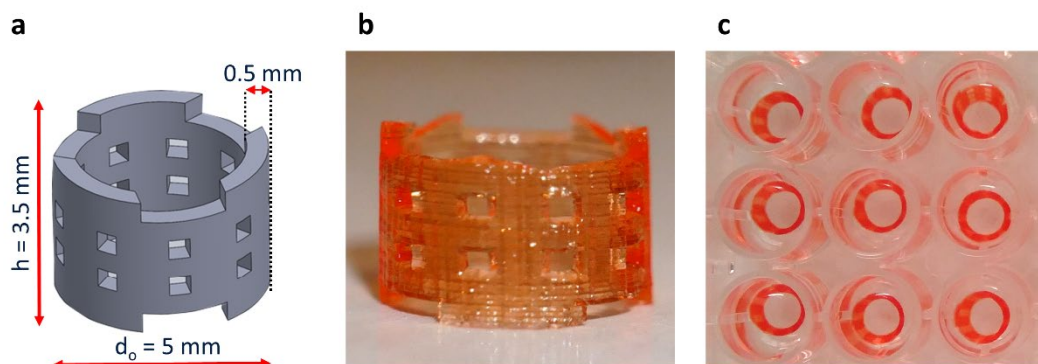
Figure 1: Printed adsorber in form of a hollow cylinder. a) CAD model, b) photograph of printed cylinder, c) cylinders in 96-microplate wells. The hollow cylinder format allows convenient measurement of the protein concentrations using a plate reader.
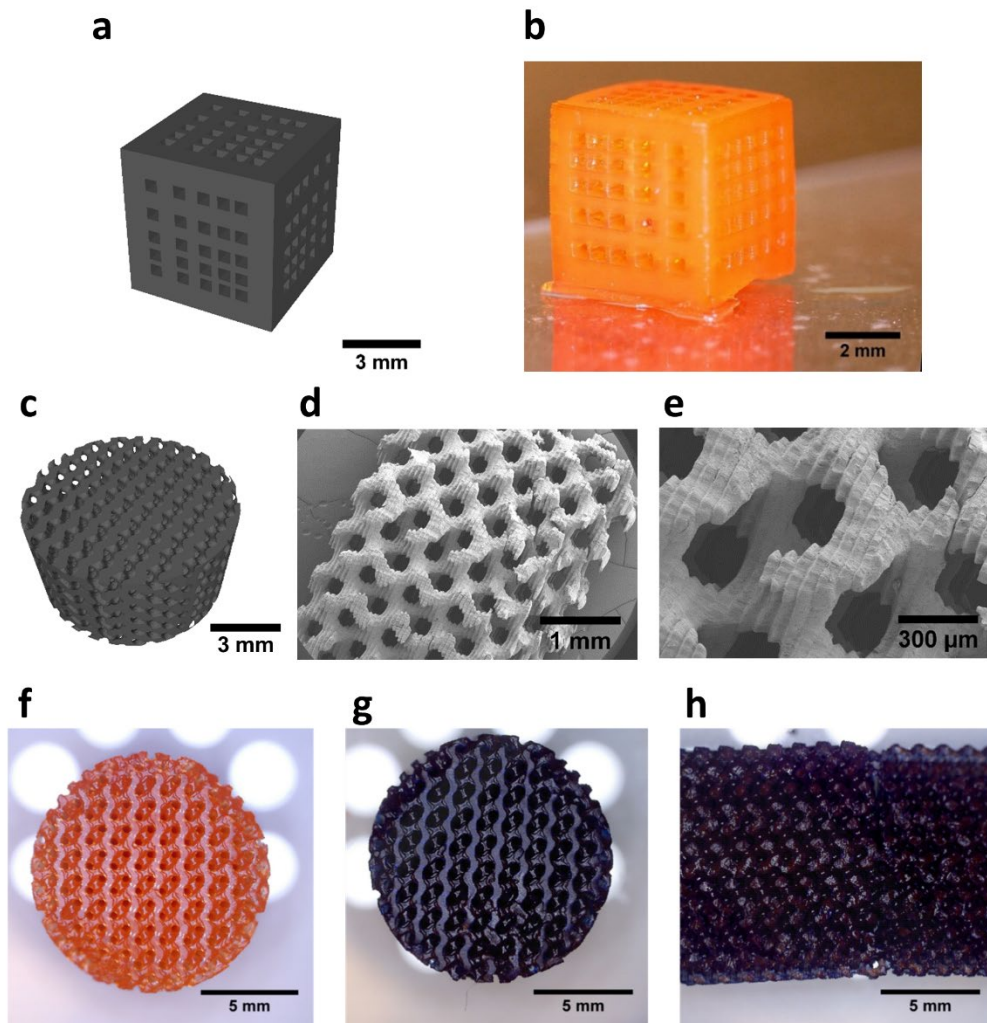

Figure 2: Chemical structures of a) PEGDA and b) AETAC.

20
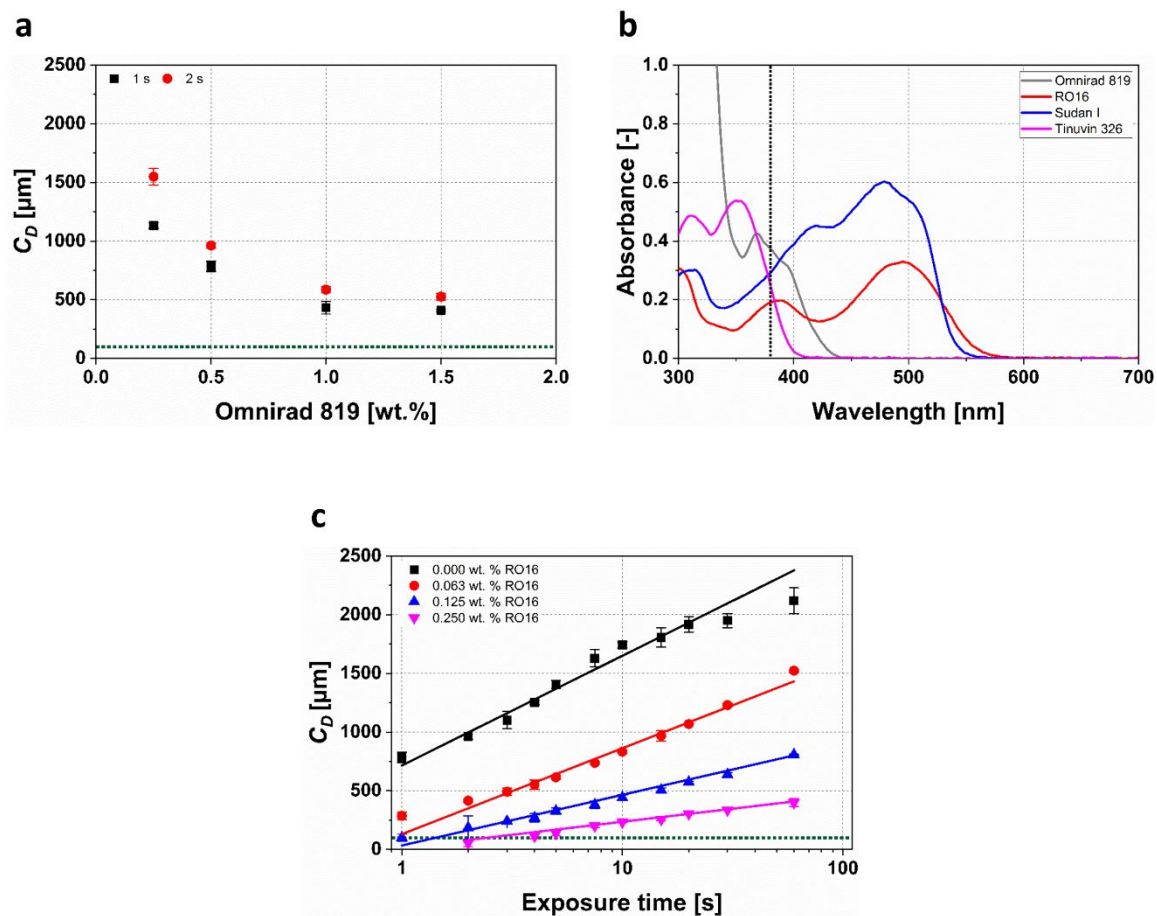
Figure 3: AEX material development. a) cure depth, C_D, as function of Omnirad 819 (photoinitiator) concentration for exposure times of 1 and 2 s. Monomer to crosslinker ratio of 14:26 (2.03 mmol/mL ligand density). b) Absorbance spectrum of Omnirad 819 (50 ppm by weight in IPA) and the analysed dyes RO16, Sudan I and Tinuvin 326 (12.5 ppm in IPA/H_2O). Printer's output wavelength was 385 nm (black dotted line). c) Working curves at different concentrations of RO16 as photoabsorber. Other components are 0.5 wt. % Omnirad 819 and monomer to crosslinker ratio of 14:26 (2.03 mmol/mL ligand density). Error bars in a) and c) correspond to standard deviation. Green dotted lines correspond to the target layer thickness of 100 μm. Fitting parameters in supplementary Table S1.

Figure 4: Testing printability, printing resolution and porous structure of the new material formulation (ligand density 2.03 mmol/mL). a) CAD model and b) photograph of test cube with 500 µm channels, separated by 200 to 1000 µm thick walls. c) CAD model and d,e) SEM images of a Schoen gyroid with a designed external porosity of 50 % and wall thickness of 500 µm. Some degree of shrinkage can be noticed as a result of drying for sample preparation. f) Photograph of printed cylindrical Schoen gyroid before and g) after 24h incubation with 1 mg/mL CPC. h) Model cut open after 24 h of incubation with 1 mg/mL CPC.
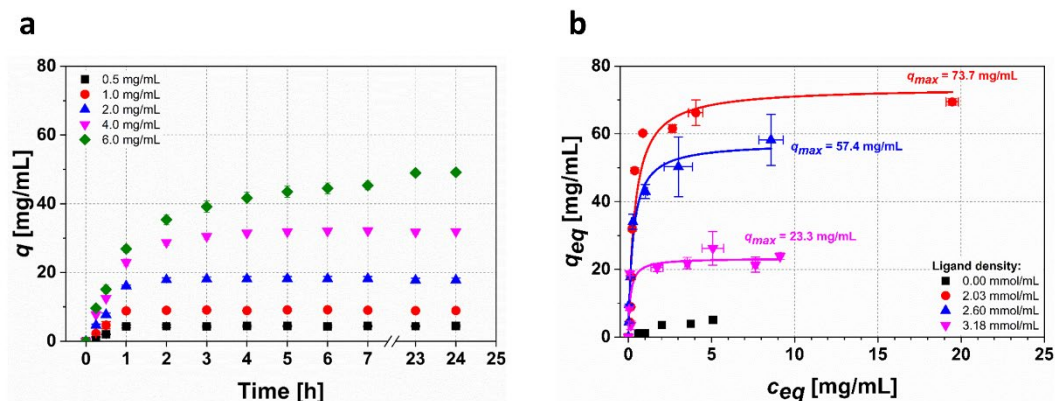
708
709 **Figure 5:** BSA batch adsorption experiments. a) Adsorption kinetics onto novel material
710 formulation with ligand density of 2.03 mmol/mL. Initial BSA concentration of 0.5 – 6 mg/mL.
711 b) Equilibrium adsorption data for the four materials tested (ligand densities of 0.00, 1.81,
712 2.32 and 2.84 mg/g). Continuous lines are best-fit according to Langmuir model. Fitting
713 parameters are listed in Table 2. Error bars correspond to standard deviation.
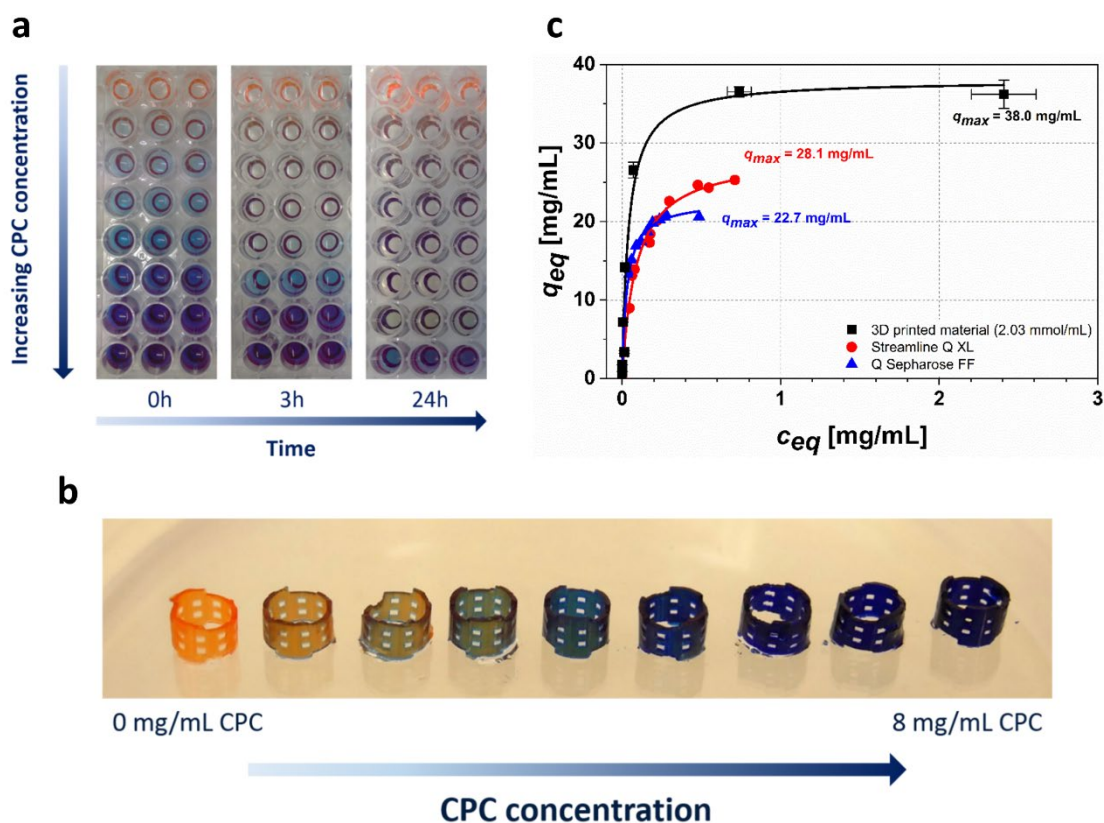
714
715 **Figure 6:** CPC batch adsorption onto novel 3D printed AEX material with ligand density of
716 2.03 mmol/mL. CPC concentration at beginning of experiment of 0.000, 0.125, 0.250, 0.500,
717 1.000, 2.000, 4.00 and 6.00 mg/ml. a) 3D printed cylinders in multiwell plate soaked in CPC
718 solutions of different concentration at 0, 3 and 24 h following incubation. b) Adsorber
719 cylinders after 24 h incubation with CPC solutions at increasing concentration. c) Comparison
720 of equilibrium adsorption data of the AEX printed material (this work), Streamline Q XL (from

23

721 [40]) and Q-Sepharose (from [31]). Continuous lines are best-fit according to Langmuir model.
722 Fitting parameters are listed in Table 2. Error bars correspond to standard deviation.

723

Supplementary material

Direct 3D printing of monolithic ion exchange adsorbers

Ursula Simon & Simone Dimartino*

Institute for Bioengineering, The School of Engineering, The University of Edinburgh,

Edinburgh EH9 3DW, UK.

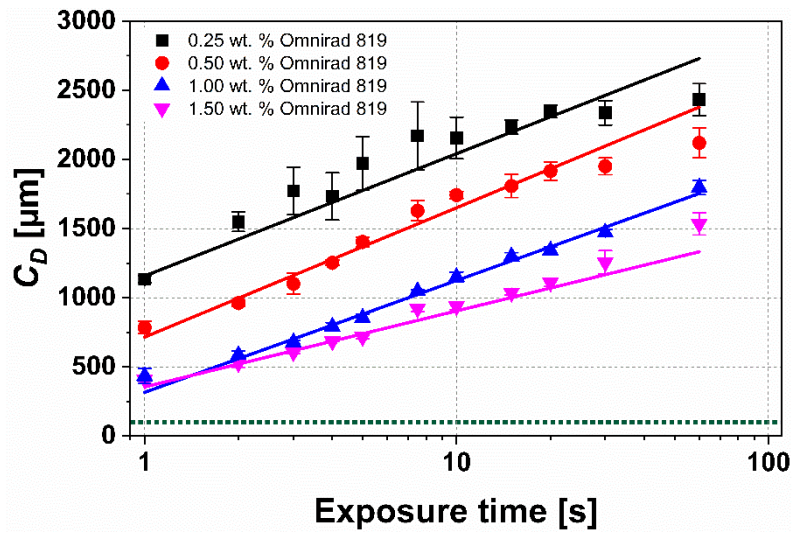*Corresponding author: Phone: +44 131 6507305, Email: simone.dimartino@ed.ac.uk

733 Table S1: Fitting parameter for working curves in Figure 3c. Curves are fitted with y=a*ln(x)+b.
734 Displayed error corresponds to standard error.

RO16 concentration [wt. %]	a [μm]	b [μm]	R^2
0.000	406 ± 25	715 ± 43	0.97
0.063	318± 16	130 ± 43	0.98
0.125	188 ± 2	33 ± 3	0.99
0.250	97 ± 6	14 ± 17	0.98

737

738

739 Figure S1: Working curves for different Omnirad 819 concentrations from 0.25 to 1.5 wt. %.
740 The green dotted line displays the target layer thickness of 100 µm. The higher the initiator
741 concentration the lower the C_D. Error bars correspond to standard deviation.
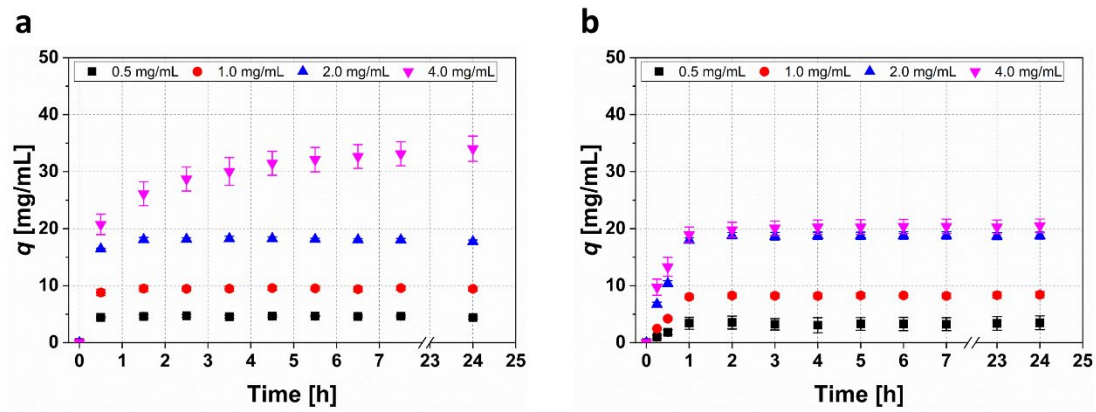
742

743

744

745

746 Table S2: Fitting parameter for working curves in Figure S1. Curves are fitted with $y=a*\ln(x)+b$.
747 Displayed error represents the standard error.

Omnirad 819 concentration [wt. %]	a [µm]	b [µm]	R^2
0.25	384 ± 18	1157 ± 33	0.98
0.5	406 ± 25	715 ± 43	0.97
1.0	351 ± 12	315 ± 24	0.99
1.5	239 ± 15	355 ± 21	0.97

748

749

750

751 Figure S2: BSA binding kinetics for the initial protein concentrations from 0.5 to 4 mg/mL BSA.
752 Displayed errors represent standard deviation. (a) Material presenting a ligand densities of
753 2.60 mmol/mL. (b) Material with ligand density of 3.18 mmol/mL.

754

755

756